Department of Physics and Astronomy
Heidelberg University

Bachelor Thesis in Physics
submitted by

Bram Everts

born in Enschede (Netherlands)

2023

Design of an edge coupler for chip to chip coupling within the QSAMIS project

This Bachelor Thesis has been carried out by Bram Everts at the
Kirchhoff-Institut für Physik in Heidelberg
under the supervision of
Erik Jung and Prof. Wolfram Pernice

1 Abstract

The objective of this bachelor thesis is to develop an edge coupler for chip-to-chip coupling within the QSAMIS project, where a SiN/Sio_2-Chip should be connected to an InP-Chip.
In the design phase, the coupler is segmented into three main sections: the transition sector, the taper, and the lens. The transition sector, essential for efficient optical power transfer from the silicon to the polymer, has undergone optimisation beforehands.
For the simulations of the coupler, the program Meep is used. With the help of Meep, separate analyses of the coupler in both xy- and xz-planes are conducted. The analyses reveals that parabolic tapers are most effective in both planes. In the xz-plane, the taper allows adiabatic expansion of the first eigenmode. Due to the layerstack, the taper in the xy-plane can only expands the light to the required taper end height. Further, the ellipsoidal lens is analyzed to achieve the targeted focal point and focal length.
Lastly, the coupler's bi-directionality is assessed. This involves positioning two identical couplers mirror revers, with one transmitting light and the other receiving the transmitted light. Thereby sufficient S21 parameters of -0.7 dB in the xz-plane and -1.25 dB in the xy-plane are measured, confirming the bi-directionality of the coupler.

2 Zusammenfassung

Das Ziel dieser Bachelorarbeit ist die Entwicklung eines Edge-Kopplers für die Chip-zu-Chip-Kopplung im Rahmen des QSAMIS-Projekts, bei dem ein SiN/SiO_2-Chip mit einem InP-Chip verbunden werden soll.
In der Analysephase wird der Koppler in drei Hauptabschnitte unterteilt: Den Übergangsbereich, den Taper und die Linse. Der Übergangsbereich, der für eine effiziente optische Leistungsübertragung vom Silizium auf das Polymer ermöglicht, wurde im Vorfeld optimiert.
Für die Simulationen wird das Programm Meep verwendet. Damit werden separate Analysen des Kopplers in den xy- und xz-Ebenen durchgeführt. Die Analyse der Taper zeigt, dass parabolische Taper in beiden Ebenen am effektivsten sind. In der xz-Ebene ermöglicht der Taper eine adiabatische Expansion der ersten Eigenmode. In der xy-Ebene kann der Taper das Licht nur bis zur erforderlichen Breite ausdehnen. Weiterhin wird die ellipsoide Linse analysiert, um den gezielten Brennpunkt und die Brennweite zu erreichen.
Zuletzt wird die Bidirektionalität des Kopplers beim Empfangen und Senden von Licht analysiert. Dabei werden zwei identische Koppler spiegelverkehrt positioniert, wobei einer das Licht sendet und der andere das übertragene Licht empfängt. Die Simulationsergebnisse weisen einen S21 parameter von -0.7 dB in der xz-Ebene und -1.25 dB in der xy-Ebene, was die Bidirektionalität des Kopplers bestätigt.

Contents

3 Introduction

The development of electronics started in the early 20th century with the invention of vacuum tubes, capacitors, resistors, and inductors [1]. These were the primary methods for controlling and manipulating of electrical energy and signals. These components, however, were bulky, energy-inefficient, and unreliable. In 1947 the first transistor was invented, replacing the need for vacuum tubes as they where more reliable and consumed less power [1]. Further advancements were driven by improvements in semiconductor materials, particularly silicon. This allowed the development of integrated circuits, where multiple electronic components were fabricated on a single piece of semiconductor material. This led to the creation of microchips and microprocessors [1]. On these chips billions of transistors can be integrated, enabling powerful computing capabilities in increasingly smaller packages.

Despite the advancements in miniaturization of the electronic components of the chip, physical limitations at the nanoscale, such as heat dissipation, quantum effects, and energy inefficiency, started to become apparent [2]. Thus seeking for other technologies such as photonic integrated circuits (PICs). Thereby optic devices like lasers, modulators, and detectors are integrated with electronic components on a single chip. This integration leads to a significant improvements in data transmission speeds and bandwidth, as optical signals can carry more data at faster rates compared to electronic signals [3]. In addition, PICs can reduce the power consumption, as optical data transmission is typically more energy-efficient than electronic transmission [3]. Moreover, linear operations, particularly matrix multiplication, can be executed more swiftly and with greater energy efficiency on PICs compared to conventional electronic circuits [4]. This is especially of importance because at current growth rate of AI, the MIT hardware program predicts that the total energy spent on computation will reach 10^{27}J by 2040 [5]. This could have devastating effects on climate change. Moreover, this amount of energy far exceeds the total energy capacity that humans are expected to be able to generate then[5].

A central issue with PICs is the efficient transmitting and receiving of light from and into the chip. Addressing this, the bachelor thesis proposes the design of an edge coupler for chip-to-chip coupling within the QSAMIS project. The design aims to connect a Sin/SiO_2 chip with an InP chip.

4 Theoretical Background

4.1 Gaussian beam in free space

The propagation of light in free space is described by two distinct models. When the beam waist is significantly larger then the wavelength of the beam, the ray model is used. In this model the light is divided into several rays. These rays are theoretical lines which direction are perpendicular to the wavefront of the light. The rays represent the direction and path along which the light travels.

When the wavelength of a beam is of the same order of magnitude as its beam waist the Gaussian beam formula is used to describe the propagation of the beam. The Gaussian beam formula is stated as follows:

$$w(z) = 2 \cdot w_0 \cdot \sqrt{1 + \left(\frac{z}{z_R}\right)^2}, \quad z_R = \frac{n \cdot \pi \cdot w_0^2}{\lambda_0} \quad [6] \tag{1}$$

Thereby w_0 is the beam waist, z is the distance from the beam waist, z_R is the Rayleigh length, λ_0 is the wavelength and n is the refractive index of the media in which the beam propagates. The following figure demonstrates how these parameters interact within the context of the formula.

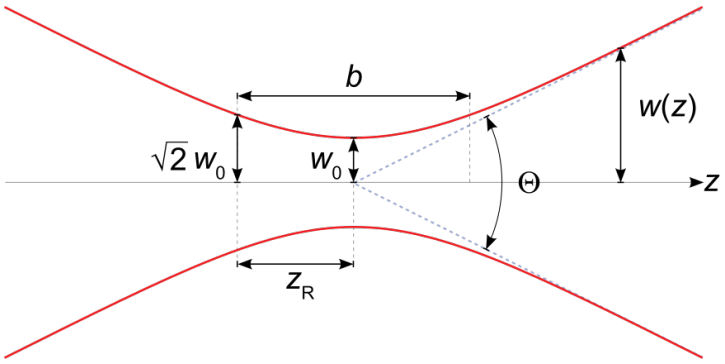

Figure 1: Visualisation of the Gaussian beam formula describing the propagation of a Gaussian beam [7]

4.2 Dielectric-Waveguide

In scenarios where the beam waist's dimension is comparable to the beam's wavelength and the light is confined within a geometric structure, unique propagation patterns can be observed. Waveguides are for instance such geometric confining structures, allowing light to propagate in one direction with freespacepropagation, while in the other directions, the light remains confined.

Waveguides have a pivotal role in the transmission of light, offering a more reliable and efficient alternative to free-space transmission. An example of such a waveguide is the planar dielectric waveguide, illustrated in figure 2. In general waveguides are composed of a core that has a high refractive index denoted as $n_1(\vec{r}, \omega)$. Here, $\vec{r}$ = (x, y, z) signifies a point in a three-dimensional space, and ω represents the angular frequency of the incoming light. The angular frequency and the wavelength are related by the equation $\omega_0 = \frac{2\pi c}{\lambda}$. The core is encased by a material with a lower refractive index, $n_2(\vec{r}, \theta)$, which is commonly referred to as the cladding.

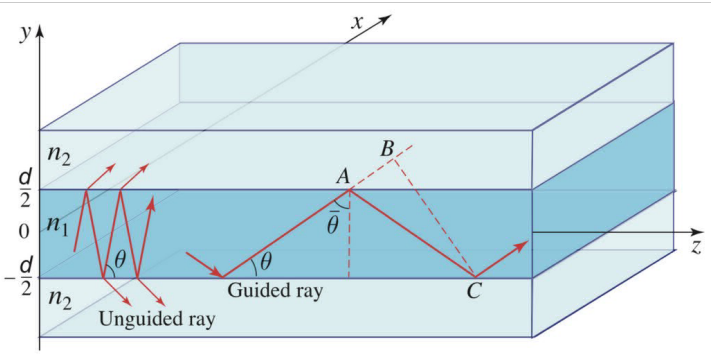

Figure 2: Illustration of a planar dielectric waveguide, demonstrating both guided and unguided light rays [6]

To describe the fundamental operating principle of a waveguide the ray model is used. The light propagation in dielectric waveguides are based on the principle of total internal reflection, which occurs if the incident light angle $\bar{\theta}$ at the core-cladding boundary is bigger then the critical angle θ_c. Due to the reflections at the core-cladding boundaries, the rays propagates along the core. These rays are called guided rays. Thereby θ_c can be calculated with the following formula:

$$\theta_c = \arcsin\left(\frac{n_2}{n_1}\right) \tag{2}$$

If the angle of incidence $\bar{\theta}$ at the core-cladding boundary is smaller then the θ_c, light is partially transmitted and partially reflected. This results in a gradual loss of light with each reflection. These rays are called unguided rays. Figure 2, depicting a planar dielectric waveguide, illustrates the distinction between guided and unguided rays.

In addition the efficiency of light transmission is affected by material absorption, especially at frequencies matching the material's electronic resonances. This can be minimized when waveguides are made from materials with absorption spectra that are far away from the transmitted light frequencies [6]. The frequency-dependent nature of the refractive index is also evident in the formula of the refractive index depicted below:

$$n_i(\vec{r}, \omega) = n_{real}(\vec{r}, \omega) + i\, k_{imag}(\vec{r}, \omega) \qquad [6] \tag{3}$$

In this equation K is called the optical extinction coefficient. It measures the light lost due to scattering and absorption as an electromagnetic wave propagates within a material.

4.2.1 Modes

The propagation of light in waveguides can be described by various modes. Modes are defined as the transverse field patterns which amplitude and polarization profiles remains constant along the longitudinal of the waveguide [6].
Propagation modes in waveguides can be distinctly categorized as Transverse Electric (TE) modes, where the electric field is oriented perpendicular to the direction of the wave propagation, and Transverse Magnetic (TM) modes, where the magnetic field is oriented transversely to the propagation direction [6].

These modes can exist in various orders, denoted as $TE_{m,n}$ or $TM_{m,n}$ where 'm' and 'n' are integers indicating the mode configuration within the waveguide [6]. The particular modes that can be supported by a waveguide depends on its dimensions and the frequency of the light. Each waveguide has a specific lower frequency limit known as the cut-off frequency. By solving the Maxwell equations

for the analysed waveguide the cut-off frequencies can be calculated. Signals with a frequency below the cut-off frequency can not propagate in the structure [6]. In addition, it is possible for multiple modes to propagate along a waveguide. The number of possible modes for a given size of structure increases with the frequency. In figure 3 modes are depicted of a cylindrical waveguide and a rectangular waveguide.

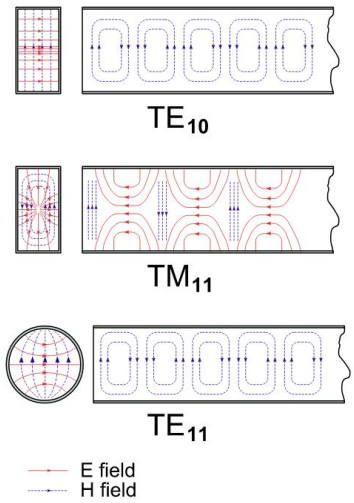

Figure 3: Field patterns of modes in a cylindrical and rectangular waveguide [8]

4.3 Integrated photonics circuits

Waveguides are also used in photonic integrated circuits (PICs), guiding light across the chip. Pics are based on intergrated circuits (IC). These are small electronic devices made up of multiple interconnected electronic components such as transistors, resistors, and capacitors. A PIC is a IC containing two or more photonic components forming a functioning circuit. These photonic components can for instance be lasers, polarizers, or phase shifters

Figure 4 illustrates the layer stack of a PIC. The foundational layer of the PIC is silicon, measuring 525 µm in thickness. By using silicon the Pics are compatible with the ICs, as silicon is also used for the IC. The second layer is made out of the

silicon dioxide (SiO_2). This layer is 3.3 µm thick and is the subtrat. On top of the chip is an layer of silicon nitride (Si_3N_4) with a layer thickness of 330nm. Silicon nitride is beneficial due to its low propagation loss and heigh refractive index [9].

Figure 4: Layer stack of a PIC, comprising of silicon nitride (Si_3N_4), silicon dioxide (SiO_2), and silicon (Si).

4.4 Technical merging of free space optics with integrated photonics

A major challenge for PICs is to efficiently transmit and receive light from and into the circuit. This process starts at the fiber array, where light is initially emitted into free space. Subsequently, a coupler is used to receive and guide the light efficiently into the PIC.

In general, one can broadly categorize current fiber-to-chip coupling concepts into out-of-plane and in-plane couplers [10]. In-plane couplers facilitate the coupling of light into waveguides either from the chip's facets or through tapered fibers that are precisely aligned with photonic structures at the edge of the chip. These couplers have a high coupling efficiencies and provide wide optical bandwidth. The disadvantage, however, is that such couplers require fulfilling tight alignment tolerances and limit access to the chip in one dimension [10]. One can also couple light to the chip out-of- plane. Thereby allowing a larger number of devices being addressed across the chip surface. This however reduces the coupling efficiency

and coupling bandwidth [10].

Both the in-plane-coupler and the out-of-plane coupler, however, have to face the problem of the mode mismatch between the optical fiber and the smaller chip integrated waveguide. The mode size conversion can be realized off chip by using lensed fibers [11], tapered fibers [12], or a lens between the chip and the fiber or on chip by employing tapering structures [13, 14]. Moreover, grating couplers [15], inverse couplers [16] and prism couplers [17] can also be used. In this thesis, an edge coupler is designed.

4.5 Simulation program Meep

The program Meep is used for simulating the light propagation in the coupler and in free space. Meep is built on the Finite Difference Time Domain (FDTD) algorithm. This algorithm discretize the Maxwell's equations in both space and time, applying them to a grid [18]. The individual cells in this grid are known as Yee cells. In these cells, electric and magnetic fields are strategically staggered, to ensure that both fields maintain a divergence-free state [18]. By doing so, the computation of the Maxwell's equations is greatly simplified, enhancing the efficiency of the simulations. In the simulation, the parameter 'resolution' determines the number of cells utilized per µm. The official Meep documentation recommends a setting of 10 $\frac{\text{cells}}{\mu\text{m}}$ to adequately capture the nuances of light propagation within the simulation [18].

5 Simulations

In this chapter, a concept for efficient chip-to-chip coupling by means of a three-dimensional polymer coupler is designed. The chapter begins by introducing a beam analyzing algorithm. Subsequently, the Gaussian beam formula is employed to calculate the desired mode field diameter at the taper's output facet. Then the desired tapers output height for the calculated mode field diameter must be determined. Therefore the correlation between the radii of a waveguide and its respective mode field diameter is analysed.

With help of the determined waveguide radii, the coupler is modeled based on two independent 2D simulations for the xy-plane and the xz-plane. For both the planes, a focusing lens is designed fulfilling design constraints explained in chapter 5.1. The layerstack results in different propagation properties especially for the taper in the two planes.

In the xy-plane, an asymmetric taper is designed, characterized by its asymmetry. This taper is incapable of expanding the first eigenmode adiabatically. As a result, the taper only expands the mode to the desired height. In contrast, within the xz-plane, a symmetric taper is to be designed. In this plane, the taper can expand the mode adiabatically.

The bi-directionality of the coupler design then is tested in both planes using two identical couplers in a mirror reverse simulation setup: Thereby the couplers ability to transmit and receive light efficiently, as indicated by the S21 parameter, is assessed.

The chapter wraps up by presenting a strategy to manage chips with varying heights by deliberately tilting the lens to produce an angled beam.

5.1 Three components of the coupler

The concept for the chip-to-chip coupling needs to work in the framework of the QSAMIS project, where a SiN/Sio_2-Chip should be connected to an InP-Chip. For that reason, the couplers need to fulfill certain requirements. One key requirement is that the bi-directionality of the coupler is given meaning it receives/transmits light efficiently from/to the indium phosphide chip. This dual functionality of the coupler, encompassing receiving both the coupling and transmission processes, is illustrated in figure 5 b by means of the green and red arrows.

The fabricated InP chip is specifically engineered for operation within the telecom C-Band. In order to ensure the couplers compatibility in the same wavelength range, all the simulations have been performed with an wavelength of λ = 1550 nm. For that reason, the wavelength dependency n(λ) can be dropped and the refractive index equals a material constant for each material. Due to the given Layerstack of the SiN/Sio_2-chip, the layer thicknesses and the respective refractive indices are set fixed. The couplers themselves are fabricated out of an polymerized, initially liquid photoresist with an refractive index of 1.54. They are located on top of an Sio_2 substrate with an refractive index of 1.44. The coupler is surrounded by air except for the side based on top of the substrate. In figure 5 a the coupler is depicted showing the refractive indices of the materials facilitated on the chip.

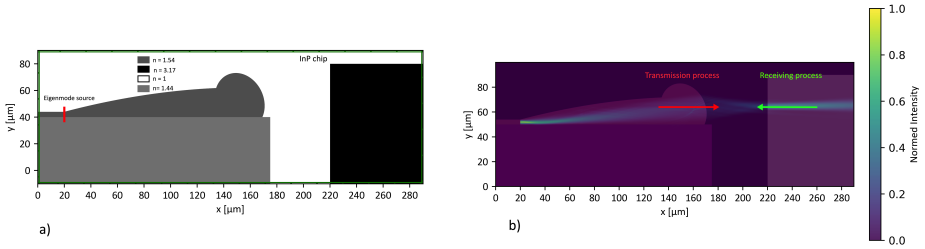

Figure 5: The sketch (a) displays a Sin/SiO_2-chip with an integrated 3D polymer chip-chip coupler and an InP chip. The bi-directionality of the coupler is represented by red and green arrows in figure (b), denoting the transmission and receiving processes respectively.

The coupler is composed of three main components. Firstly, there is a transition section that facilitates the transfer of the optical power efficiently from the SiN to the Polymer waveguide. Secondly, a taper is incorporated to widen the mode field diameter. Lastly, a lens is included in the design to focus the light, ensuring an appropriate spot size and focal length.

The power transfer from the SiN waveguide to the Polymer waveguide is realized by tapering the two waveguide in reverse directions. Due to the resulting change in the effective refractive index, the mode is adiabatically transferred from the SiN waveguide into the Polymer. Figures 6 a and 6 b demonstrate the top and side view of the silicon-to-polymer transition. This transition was optimized beforehands resulting in an experimentally measured loss of approx 0.15 dB, as depicted in graph 6 c. The resulting polymer waveguide possesses the cross-section of 4x4 µm. This was used as the starting point of the optimization.

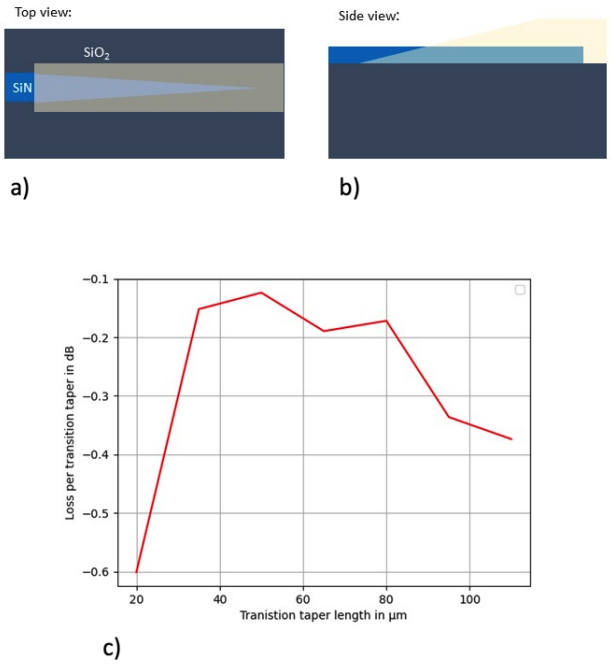

Figure 6: a and b depict the top and side views of the silicon-to-polymer transition. The graph (c) illustrates the light loss at the transition in relation to the transition taper length.

A taper expanding the first eigenmode forms the second component of the coupler. Within the xz-plane, this expansion is implemented symmetrically. However, the expansion process differs in the xy-plane due to the constraints posed by the presence of a substrate. In this plane, the expansion must be asymmetrically to accommodate the spatial limitations imposed by the substrate. Furthermore, it is essential that the coupler, comprising both the taper and lens, is designed to fit within a maximum size of 150 µm. This constraint results out of the 200 µm write field size of the used 3D printer.

The InP incoupling facet is designed for a beam with an incoming mode field diameter of 11 µm along the z-axis and 6 µm along the y-axis. For an efficient chip-to-chip coupling, the transmitted beam needs to posses the same properties at its focal point. Figure 7 depicts the desired cross section of the focal point. As the two chips need to be glued right next to each other, which can be done with 30 µm distance in between the two chips. In order to safely gap the distance between the two chips, the coupler requires a focal distance of 50 µm. Figure 8 presents a detailed SEM image showing the two chips precisely positioned 50 µm apart.

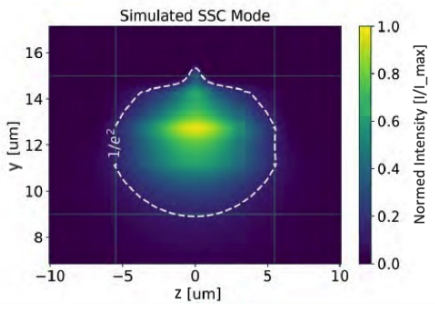

Figure 7: Cross-section of the desired laser beam at the focal point

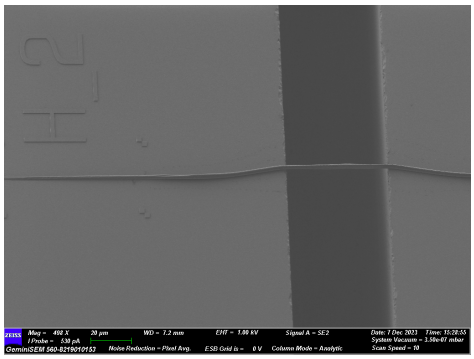

Figure 8: SEM image of the two chips precisely positioned 50 µm apart

The propagation of light in the xz-direction and in the xy-direction is linearly independent. Therefore the simulation of the 3D coupler can be split in two 2D simulations of the respective cross-sections. In both simulations, it is essential that the coupler maintains consistent length to ensure a uniform 3D coupler without any overlap.

At the commencement of the analyses, the resolution of the simulation was analysed to balance the need for precise accuracy with the practicality of simulation time. To identify the optimal resolution, the resolution is varied while the S21 parameter of a symmetrical linear taper is measured. The S21 parameter is the ratio between the first eigenmode at the entrance to the exit of the taper. The analysed linear symmetrical taper has an begin width of 0.5 µm to a terminal width of 12 µm and is 400 µm long. According to the paper [19], this taper can adiabatically expand the first eigenmode. The resolution adjustments were focused on determining the point at which the S21 parameter, reaches a value of 0. As depicted in Figure 9, the S21 parameter values converge to 0 once the resolution exceeds 20 $\frac{\text{cells}}{\mu\text{m}}$, indicating effective adiabatic expansion of light through the taper. Consequently, a resolution of 20 $\frac{\text{cells}}{\mu\text{m}}$ was established as sufficient for the following simulations.

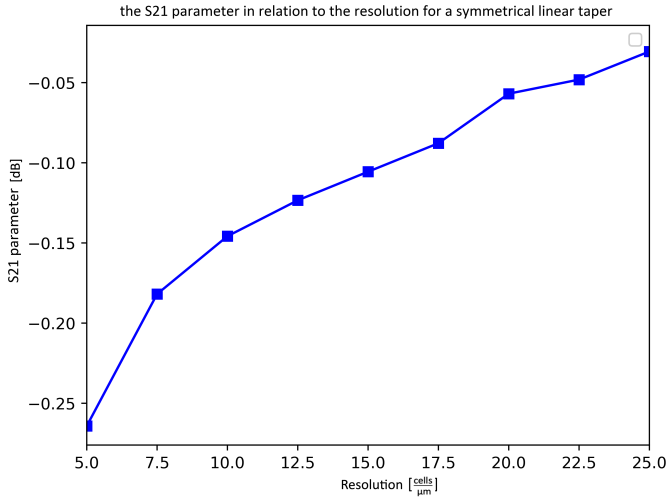

Figure 9: Varying the resolution and measuring the S21 parameter in a symmetrical linear taper to identify the resolution at which the S21 parameter stabilizes

5.2 Beam analysis technique

An algorithm is then designed to analyze the light intensity in free space and within the coupler. The primary objective is to determine the focal width and focal length of a beam. To illustrate the algorithm, the beam shown in figure 10 a is examined. Initially, a threshold process is applied, where each cell with an intensity value surpassing $\frac{1}{e^2}$ of the peak intensity is assigned a value of 1, while all other pixels receive a value of 0, resulting in the binary beam shown in figure 10 b. with help of the binary beam the propagation axis can be calculated. Subsequently, the algorithm slices the beam vertically along its propagation axis.

To each cross-sectional slice, a Gaussian fitted to the intensity profile. This Gaussian fit enables the calculation of the beam's width at that specific slice. Figure 10 d illustrates the intensity profile and its corresponding Gaussian fit at the beam's focal point.

In figure 10 c, the corresponding beam profile is depicted. Within this plot, each calculated beam width is plotted against the position of the slice. The focal point in this plot is where the beam width is minimal.

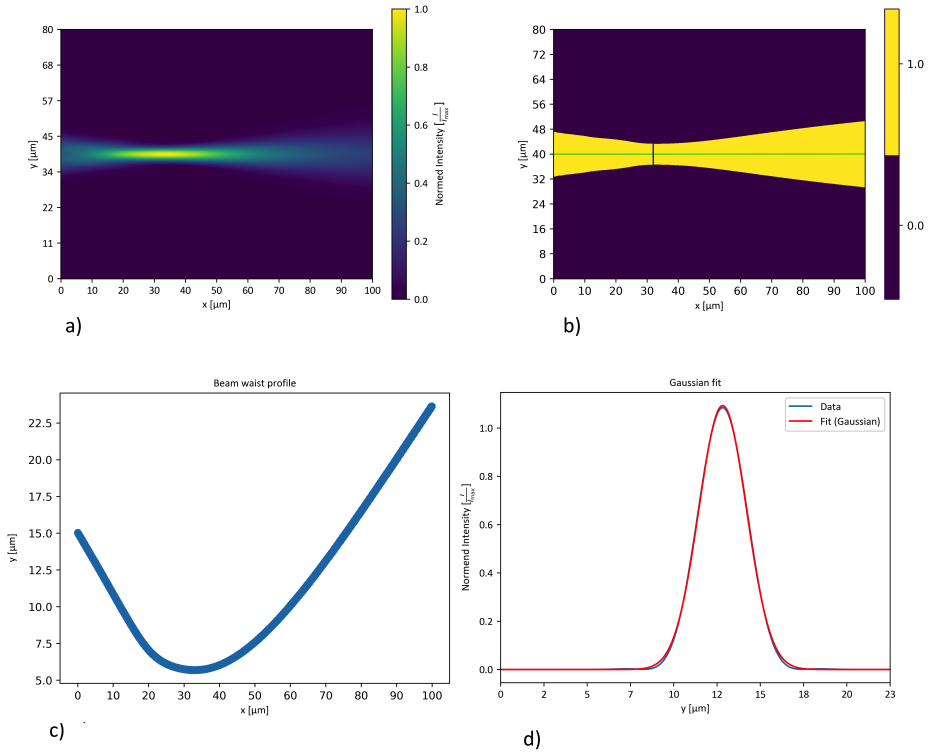

Figure 10: Part (a) showcases the analysed beam. Segment (b) displays the beam's binary representation with cells with an intensity greater than $1/e^2$ assigned a value of 1. This segment features a green line to indicate the direction of beam propagation and a black line to represent a slice taken from the beam. In segment (c), the beam width is depicted in relation to the x-axis. Finally, segment (d) illustrates the Gaussian fit applied to the intensity profile at the focal point.

5.3 Determining the desired taper end height

As mentioned in chapter 5.1, the bi-directionality of the coupler is essential for efficient chip-to-chip coupling. Consequently, the mode field evolution for the free-space propagation in between the lens and the focal point is calculated by means of the Gaussian beam formula 1.

For the xz-plane, the coupler must have a beam with a focal width of 11 µm. Application of the Gaussian beam formula under these parameters yields a mode field diameter of 14.2 µm at the lens. A parallel approach is adopted for the xy-plane, where the focal width should be 6 µm. Subsequent calculations using the formula indicate that the mode field diameter at the lens should be 17.5 µm.

To determine the desired taper end height, the relationship between the mode field diameter and the taper end height is analysed. Thereby the diameter of a waveguide is varied and the corresponding mode field diameter is measured. Figure 11 illustrates this relation. For a waveguide height of 18.2 µm, the corresponding mode field diameter in the xz-plane measures 14.2 µm. Conversely, when the mode field diameter in the xy-plane is 17.5 µm, the waveguide height must be 22.2 µm.

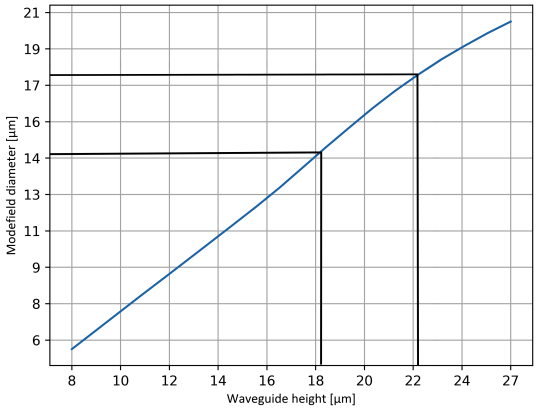

Figure 11: Establishing the relationship between the height of the waveguide and the diameter of the mode field to accurately determine the optimal end taper height.

5.4 2D design of the coupler in the xz-plane

5.4.1 Lens analysis in the xz-plane

Building upon the insights gained from chapter 5.3, it is acknowledged that the taper end height is fixed at 18.2 µm in the xz-plane. Consequently the lens in the xz-plane can be designed. The ellipsoidal lens is defined by the semiaxis a_{xz} and b_{xz}. A sketch of this lens is depicted in figure 12.

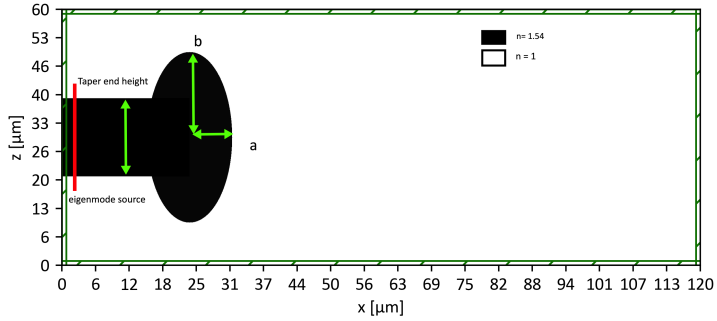

Figure 12: Sketch illustrating an ellipsoidal lens in the xz-plane, defined by its a_{xz} and b_{xz} axes, and the taper end height

Determining the precise dimensions for the a_{xz} and b_{xz} axes is fundamental to achieving the targeted focal width and focal length. To this end, iterative adjustments of the a_{xz} and b_{xz} axes were made to observe their effects on the beam's focal length and width respectively. The simulation results are depicted in figure 13 a. The red curve highlights the lenses with a focal length of 50 µm.

Subsequently in figure 13 b, the lenses with a focal length of 50 µm are plotted against there focal widths. In figure 13 b, it is evident that the b_{xz} axis must be 16.5 µm as then the focal width is 11 µm. Utilizing figure 13 a, it is deduced that for an b_{xz} axis of 16.5 µm, the corresponding a_{xz} axis must be 6 µm to achieve a focal length of 50 µm.

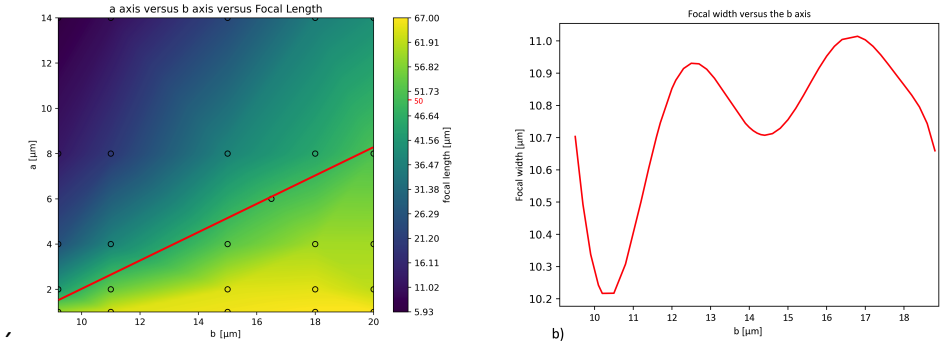

Figure 13: Illustration (a) depicts the correlation between the a_{xz} and b_{xz} axes of the ellipsoidal lens and the focal length. The red curve highlights lenses that have a 50 µm focal length. In figure (b) the b_{xz} axes of the lenses with an focal length of 50 µm are depicted with their focal widths

5.4.2 Adiabatic symmetric mode expansion

For the adiabatic expansion of the first eigenmode in the xz-plane, the symmetric tapers are analyzed. The goal is to determine the most effective taper design, considering the limitations imposed by the 3D printer's write field, restricting the coupler's length to 200 µm. Considering the transition section from SiN to Polymer and the lens size, tapers with lengths up to 130 µm are analysed. Therefore there is still adequate space for integrating the lens within this constraint.

To evaluate the efficiency of a taper, the S21 parameter, a ratio of the power flux of the first eigenmode at the taper's entrance to its exit, is measured. In figure 14 the simulation setup reference of the S21 measurement of a symmetric parabolic taper is depicted. The flux of the first eigenmode is measured by mode monitors depicted as blue stripes in the simulation setup reference. Futhermore, the first eigenmode is emitted by an eigenmode source illustrated as a red stripe.

In general a taper can be defined by three key parameters as depicted in figure 14. h_b represents the begin height of the taper, while l denotes the distance over which the taper extends. Finally, h_e is the height to which the taper expands to.

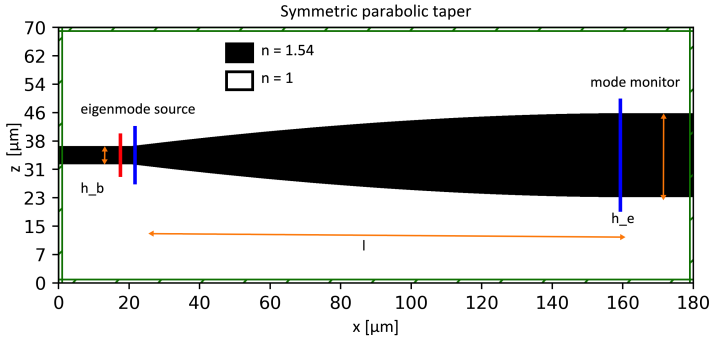

Figure 14: Sketch of a symmetric parabolic taper illustrating the simulation setup reference for the S21 parameter measurement and depicting the key parameters of a taper

Initially, a linear taper, proposed in the paper of Fu and Yunfei [19], is examined. This taper is characterized by a uniform change in the cross-section, offering a straightforward approach to the eigenmode expansion.

In the same paper a Gaussian beam is also analysed [19]. This taper is based on the Gaussian beam formula 1, which is essential for describing the propagation of the Gaussian beam in free space. The mathematical representation of the Gaussian taper is as follows:

$$h(x) = h_b \cdot \sqrt{1 + \left(\frac{x}{z_R}\right)^2} \tag{4}$$

In this context, z_r represents a parameter used to adjust the taper end height. Moreover, a parabolic taper was also analysed. This taper is inspired by the paper of Burns [20]. Thereby the parabolic taper is defined as follows:

$$h(x) = \frac{(h_b - h_e)}{l^m} \cdot (l - x)^m + h_e \tag{5}$$

For each parabolic taper, the end height is adjusted to different 'm' values, and the corresponding S21 parameter is measured. Figure 15 depicts the optimal m value for each h_b. Thereby it is evident that the m value must be 1.7 for an parabolic taper with an h_b of 18.2 µm.

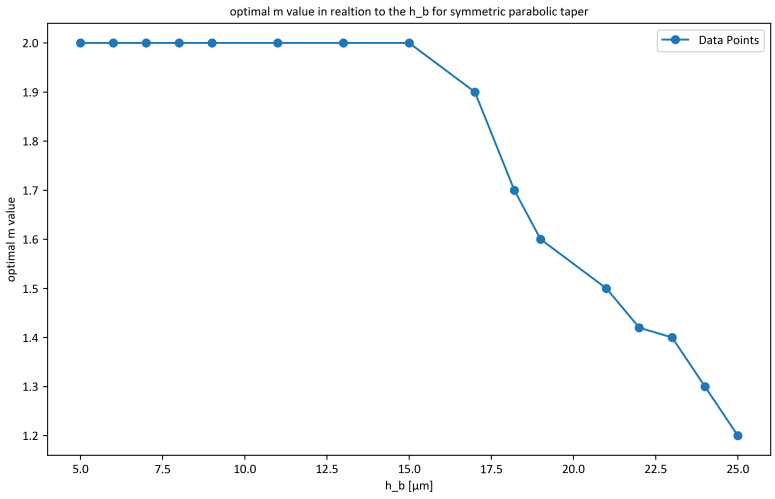

Figure 15: Optimal m value for the symmetrical parabolic end taper height

Figure 16 depicts the S21 parameter of the different taper geometries. Thereby the parabolic taper demonstrates superior performance. At a taper end height of 18.2 µm an S21 parameter of -0.1 dB is achieved. Consequently, the parabolic taper is chosen for the coupler in the xz-plane. In addition, figure 16 also depicts the three different tapers.

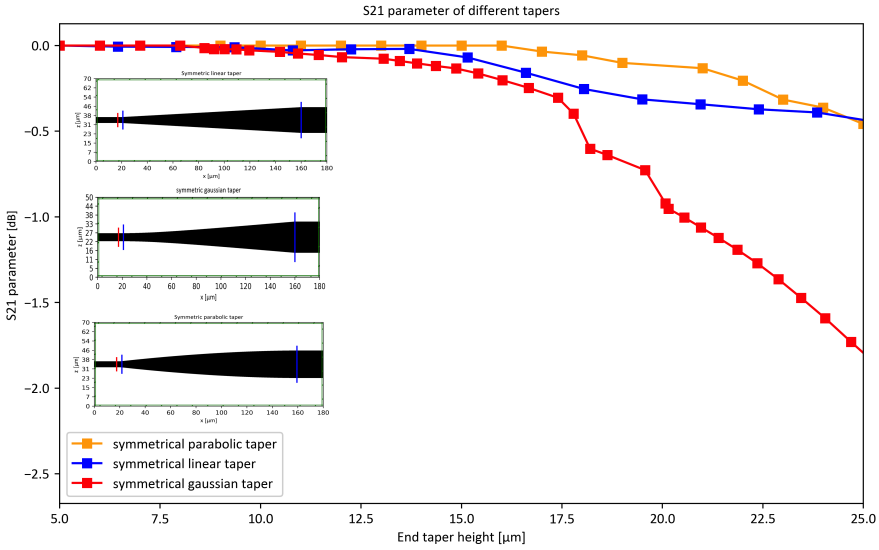

Figure 16: Comparative analysis of the S21 parameters across various symmetrical tapers in relation to the taper end height, featuring a Gaussian taper, a linear taper, and a parabolic taper

5.4.3 Concluding 2D design in the xz-plane

A coupler with the desired focal length and focal width in the xz-plane can be realised by combining the adiabatic mode field expansion and the lens. Thereby the lens has an a_{xz} axis of 6 µm and and a b_{xz} axis of 16.5 µm. For the adiabatic mode field expansion a parabolic taper is used which can expand the eigenmode adiabatically to an height of 18.2 µm. The m value of this parabolic taper is 1.7. The designed xz-plane coupler is illustrated in figure 17 a, with its corresponding simulation presented in figure 17 b.

To ensure the design's accuracy the beam profile was analyzed in figure 17 c. It is clearly observable that the focal width is 11 µm and the focal length is 50 µm, demonstrating the precise focusing capability of the lens. Additionally, as confirmed in figure 17 d, the Gaussian fit aligns well with the intensity profile at the focal point.

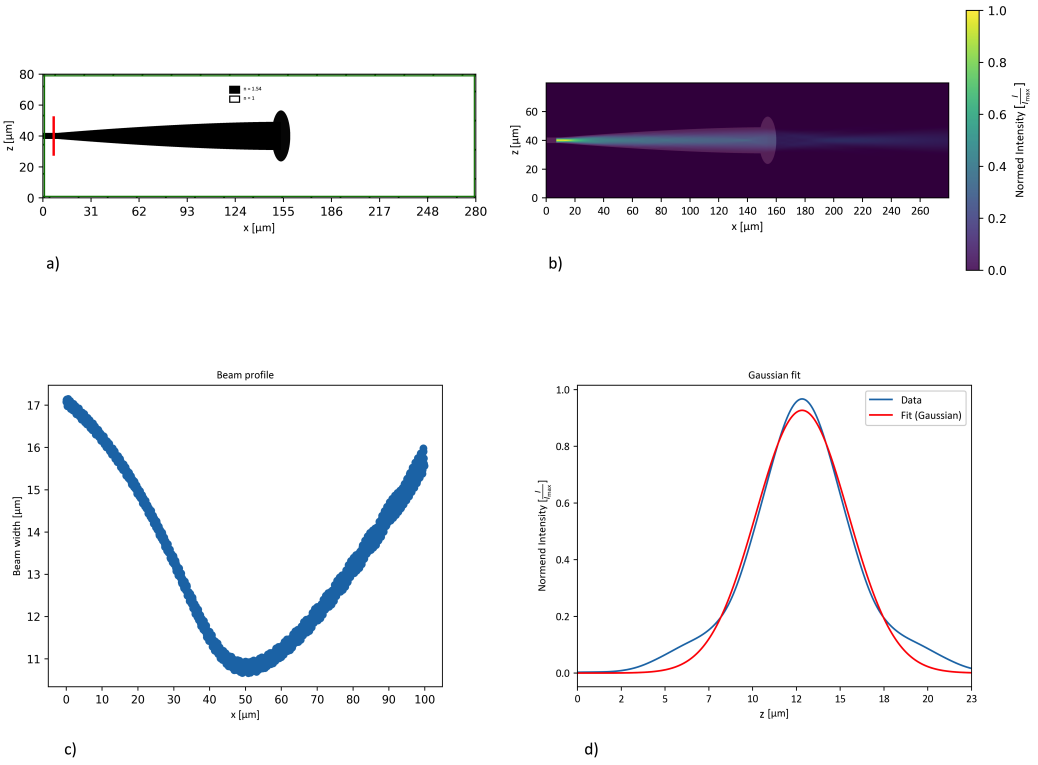

Figure 17: The sketch and simulation (a, b) depict the coupler's design and light propagation in the xz-plane, while the beam profile and Gaussian fit (c, d) illustrate the couplers beam characteristics and focusing precision at the focal point.

5.4.4 Analyses of the bi-directionality in the xz-plane

Then the bi-directionality of the coupler in the xz-plane is tested. Thereby two identical couplers are simulated mirror reverse to effectively evaluate the bi-directional capabilities of the coupler. In figure 18 the simulation setup reference is depicted.

The couplers are positioned 100 µm apart, a distance that is twice the focal length, allowing the transmitted beam to propagate effectively between the couplers. Following this simulation setup, a S21 parameter of -0.7 dB is determined. This high S21 parameter indicates the couplers high efficiency in receiving and transmitting of light, confirming the bi-directionality of the coupler.

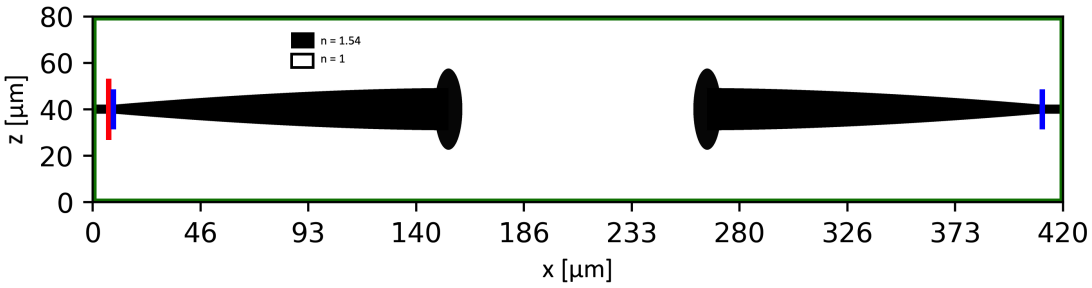

Figure 18: Simulation reference setup to evaluate the bi-directionality of a coupler in the xz-plane by measuring the ratio of transmitted to received light between the couplers

5.5 2D design of the coupler in the xy-plane

5.5.1 asymmetric mode expansion

As the parameters for the coupler in the xz-plane are determined, the coupler has to also be designed in the xy-plane. The lens in the xy-plane must have a focal width of 6 µm with a focal length of 50 µm. In addition, the taper in the xy-plane should have an end taper height of 18.2 µm as then the mode field diameter measures 14.19 µm.

Analog to the taper analyses in chapter 5.4.2, the S21 Parameter of an linear, parabolic and gaussian taper have been measured. The end taper height along with the corresponding S21 parameters are presented in figure 19.

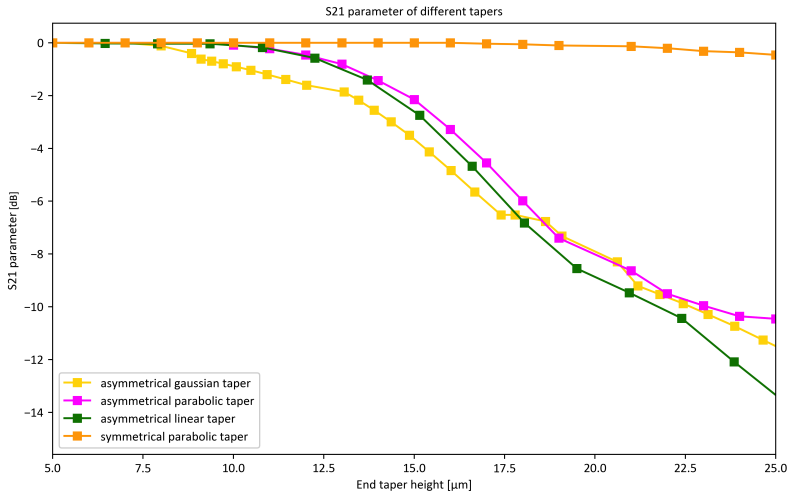

Figure 19: S21 parameters of the different symmetrical and asymmetrical tapers versus the taper end height

Figure 19 distinctly illustrates that for every taper end height the symmetrical tapers excel in performance over the asymmetrical tapers in terms of adiabatically expanding the first eigenmode. This can be attributed to the difference in geometry, as the slope of the asymmetrical one is twice the slope of the symmetrical taper. A reduced slope aids in a more gradual and controlled expansion of

the eigenmode, thereby minimizing abrupt transitions that could lead to higher modes being excited.

In contrary to symmetrical tapers, the interaction of light with the substrate has an significant influence on the mode propagation in asymmetrical tapers. This leads to the reflection of light, changing the propagation direction of light. Due to the interaction with the substrate, the propagation direction of the light is slightly changing. On the other hand, the beam is maintaining its Gaussian single-moded form. This change in the propagation direction causes an significant decrease in the S21 parameter, as the propagating beam is not any more an eigenmode of the waveguide. In chapter 5.3 a taper end height of 22.2 µm was determined. Analyzing figure 19 one can see that none of the asymmetrical tapers can expand the first eigenmode adiabatically to the desired height.

The relatively low S21-parameter is not significant in this case because after the beam passes through the lens, it will propagate in free space rather than in a waveguide. Therefore, if the coupler meets other key criteria, such as having an appropriate mode field diameter, the efficiency of chip-to-chip coupling should remain high.

For the asymmetric taper a parabolic taper was selected due to its superior S21 parameter in comparison to the other tapers. In Figure 20, the mode field diameter along the the asymmetric parabolic taper with an m value of 1.9 and an end taper height of 22.2 µm is displayed. This figures confirms that the taper achieves the desired mode field diameter of of 17.5 µm at the tapers end facet. Therefore this parabolic taper is used for the coupler in the xy-plane.

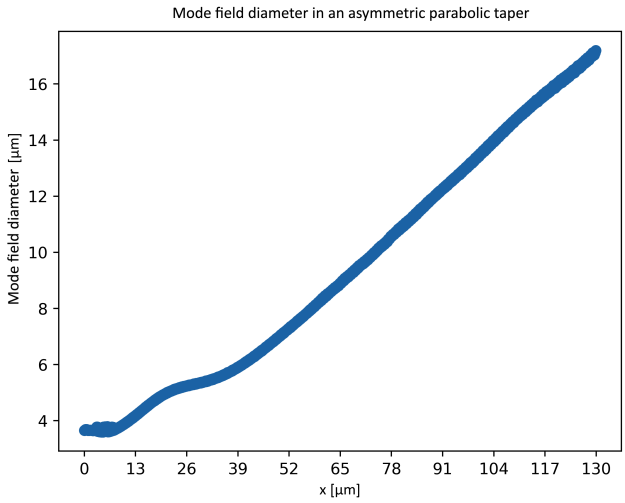

Figure 20: Illustration of the mode field diameter in the parabolic symmetric taper with an m value of 1.9, demonstrating that at the end facet of the taper, the mode field diameter is 17.5 µm

5.5.2 Tilting the lens

As mentioned in chapter 5.5, the beam is redirected due to the interaction with the substrate. To compensate for this angle, the lens must be tilted accordingly.

Exploiting Snell's law, which describes the relationship between the angles of incidence and refraction in two different media, the tilt angle of the lens is determined. From figure 21 the angle under which the ray impinge onto the surface normal is determined to 9 degree. The geometric considerations are described by figure 21 b. γ represents the angle of the light rays while β denotes the tilt angle of the lens. θ_1 and θ_2 correspond to the angles of incidence and refraction, respectively. Based on this geometric analysis the equations 7 ,8 , and 9 are derived.

$$n_1 \cdot \sin(\theta_1) = n_2 \cdot \sin(\theta_2) \quad (6)$$

$$\alpha + \beta = 90 \quad (7)$$

$$\theta_2 - \gamma = \theta_1 \quad (8)$$

$$\alpha + \theta_2 = 90 \quad (9)$$

By solving these equations, the desired lens tilt angle β can be determined. For the coupler in the xy-plane , the calcualted lens tilt is 25 degrees. Figure 21 c illustrates a coupler with a tilt of β degrees. The ellipsoidal lens used for this coupler is characterized analogous to the lens in the xz-plane by its a_{xy} and b_{xy} axes.

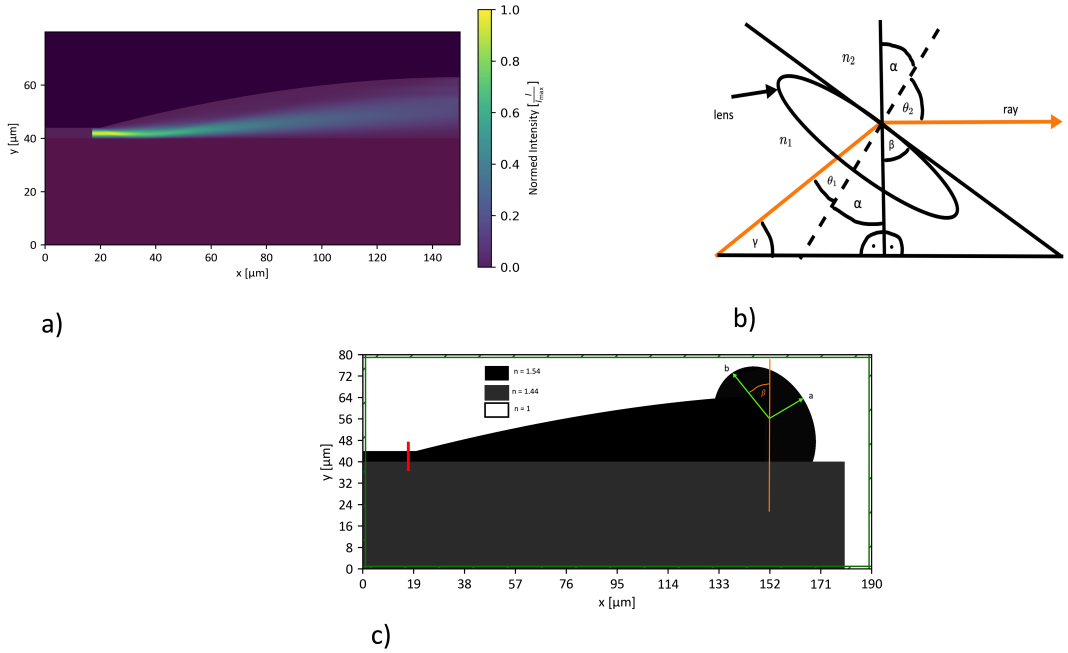

a) b) c)

Figure 21: (a) depicts the simulation results of a parabolic taper for determining the propagation-expansion angle, complemented by a geometric analyses (b) of the rays and the lens tilt to ensure a horizontal beam, and a sketch (c) showing the tilted coupler in the xy-plane.

Then the a_{xy} and b_{xy} axes are varied, while the focal length and focal width is measured. Thereby the eigenmode is expanded by the asymmetrical parabolic taper with an m value of 1.9. In Figure 22 a, the relationship between the focal length of the lens and its a_{xy} and b_{xy} axes is depicted. Thereby the red curve highlights the lenses with a focal length of 50 µm. Following this, Figure 22 b plots the lenses with a focal length of 50 µm against their focal widths. From this data, it is observed that a lens with an b_{xy} of 22 µm corresponds to a focal width of 6 µm. Additionally, Figure 22 a depicts that for achieving the desired focal width of 50 µm, the a_{xy} axis should be 18.5 µm when the b_{xy} axis is maintained at 22 µm.

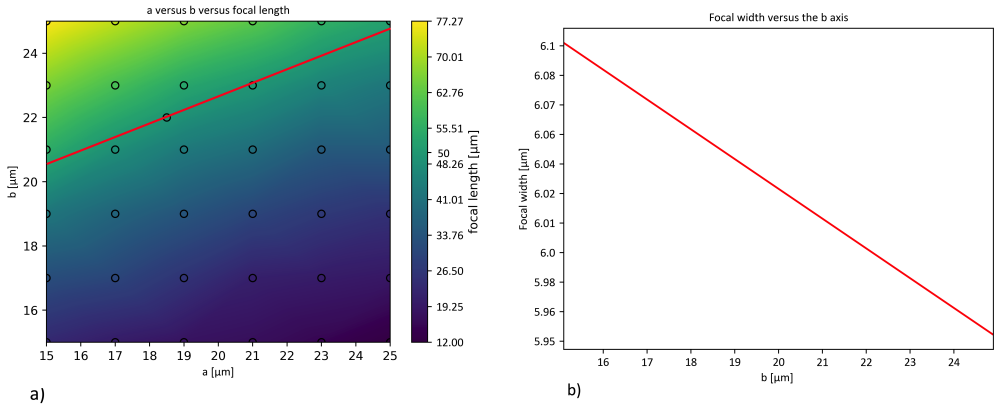

Figure 22: a) Correlation between both axes of the lens and the focal length. A red curve highlights those lenses that have a focal length of 50 µm. b) Lenses with a focal length of 50 µm are plotted with their b_{xy} axis against their corresponding focal widths to find the lens with the desired focal width.

5.5.3 Concluding 2D design of the coupler in the xy-plane

The design of the optimal coupler in the xy-plane incorporates the analyzed asymmetrical parabolic taper, which is employed to effectively expand the light. Additionally, the coupler design integrates the specifically tailored lens, distinguished by it's a_{xy} axis of 18.5 µm and a b_{xy} axis of 22 µm. Furthermore, the lens is tilted

at an angle of 25°.

Figure 23 a depicts the optimal coupler and figure 23 b illustrates the corresponding simulation of this coupler. Upon examining the beam profile in figure 23 c, the desired focal length of 50 µm and a focal width of 6 µm is confirmed. Complementing this, figure 23 d presents the corresponding Gaussian fit at the focal point, showing that the gaussian fit fits on the intensity profile.

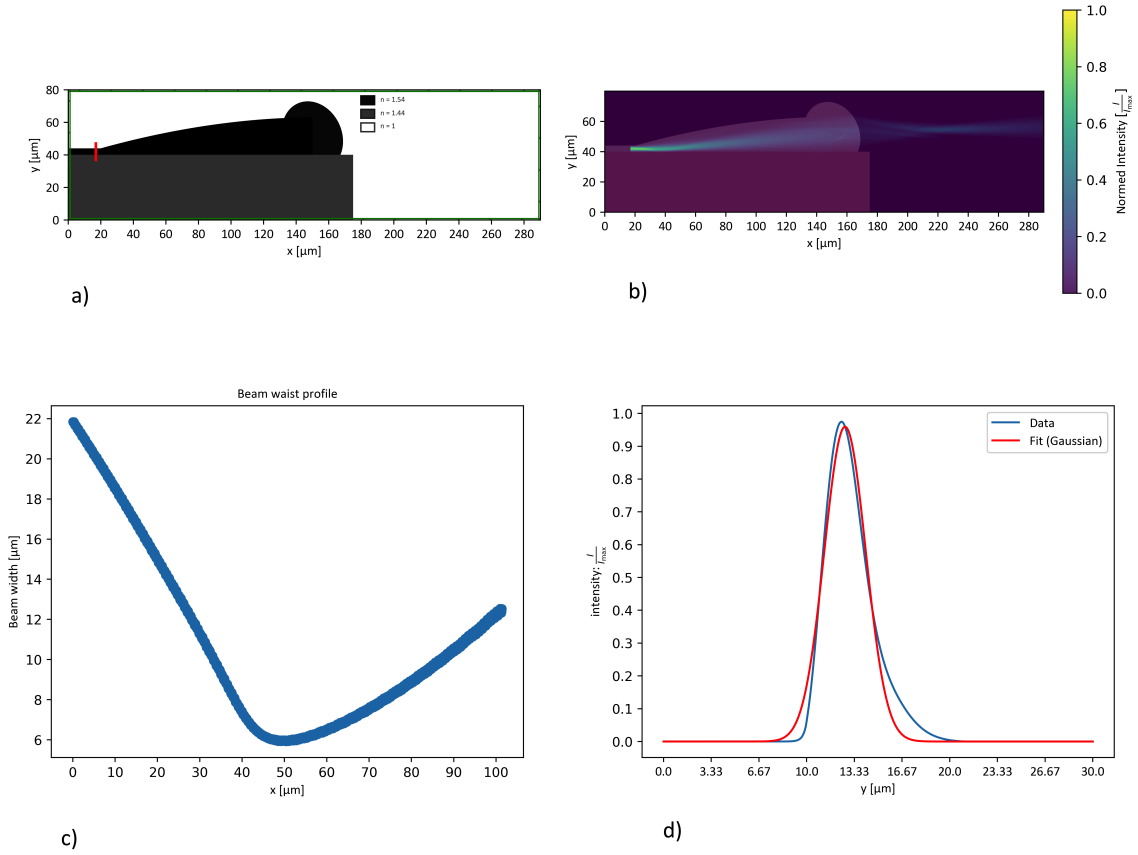

Figure 23: a) Sketch of the coupler in the xy-plane b) Simulation of the coupler in the xy-plane c) Beam profile of the coupler in the xy-plane d) Gaussian fit at the focal point

5.5.4 Analyses of the bi-directionality in the xy-plane

Then the bi-directionality of the coupler in the xy-plane has to be analysed. This is done analog as in chapter 5.4.4. In figure 24 the corresponding simulation setup reference is depicted. Thereby an S21 parameter of -1.25 dB is achieved, indicating the couplers high efficiency in receiving and transmitting of light. Due to this high S21 parameter the bi-directionality of the coupler in the xy-plane is confirmed.

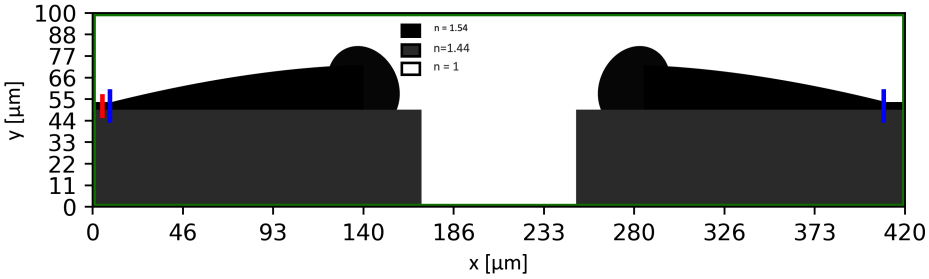

Figure 24: Simulation reference setup to evaluate the bi-directionality of a coupler in the xy-plane by measuring the ratio of transmitted to received light between the couplers

6 Modelling the 3D Coupler based on the two 2D designs of the coupler

The design of the coupler has been developed for both the xy-plane and xz-plane. To transform these 2D designs into a three-dimensional model, Blender, a 3D modeling software, is utilized. The resulting three-dimensional model of the coupler is depicted in Figure 25.

Figure 25: Transforming the 2D designs in the xy-plane and xz-plane in a three dimensional coupler

7 Bridging height disparities between the two chips

A pertinent problem arises when the external fiber-optic network and the PIC do not align along the same vertical axis. In such situations, adjusting the lens tilt, offers a remedy. Consequently the lens is tilted while the focal point is analysed. In figure 26 the lens tilt and the corresponding focal point is depicted.

When the lens is oriented at a tilt angle of -25°, the resulting beam is aligned straight. Altering this tilt angle has a direct effect on the vertical positioning of the focal point: a decrease in the tilt angle results in an upward shift of the focal point, whereas an increase in the tilt angle causes the focal point to move downward. The lens's tilt adjustment is operational within a range from -35 ° to -15 °. Within these limits, variations in the tilt angle modify the vertical position of the focal point without changing the lens's focal length drastically. This adjustment enables a vertical displacement of the focal point within a range of +2 µm to -1.75 µm.

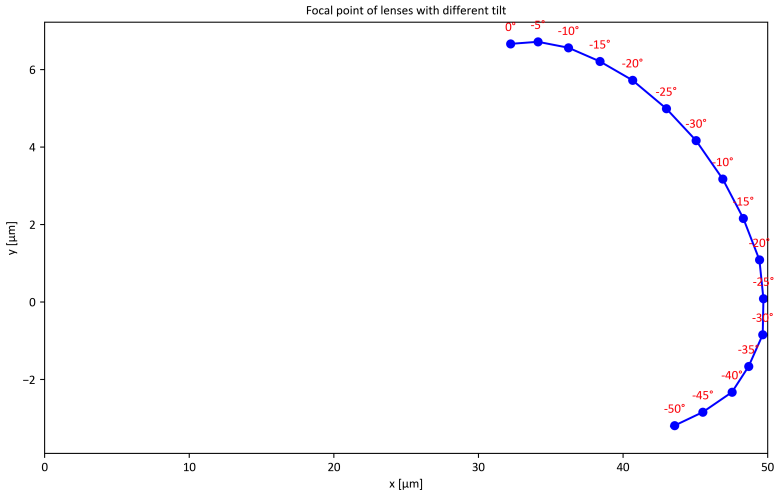

Figure 26: Adjusting the lens angle to vertically shift the focal point, compensating for height differences between the two chips

8 Conclusion and Discussion

For the QSAMIS project, a chip-to-chip coupling concept has been designed, receiving and transmitting light between a SiN/Sio_2-chip and a InP chip. During the design process the coupler was divided in three components: the silicon-polymer transition, the taper, and the lens. This thesis primarily focused, on the optimization of the taper and the lens. A parabolic asymmetric taper was engineered to expand the first eigenmode in the xy-plane. For the xz-plane, a corresponding parabolic symmetric taper was developed which can adebeitcially expand the first eigenmode. Thereby the symmetric taper has a m value of 1.7 and the asymmetric taper a m value of 1.9. In addition, the lens was designed to achieve a focal length of 50 µm and a focal width of 6 µm in the xy-plane and 11 µm in the xz-plane. Therefore, in the xy-plane, the lens has semi-axes with lengths of a_{xy} 18.5 µm and of b_{xy} 22 µm. In the xz-plane the semi-xaxis of the lens is a_{xz} 6 µm and b_{xz} 16.5 µm.

To assess the bi-directional capabilities of the coupler, two identical couplers were tested for both transmission and recieving of light. Thereby an S21 parameter of -0.7 dB in the xz-plane and of -1.25 dB in the xy-plane is measured. The high S21 parameters demonstrate the couplers exceptional effectiveness in coupling and receiving of light.

Despite the high S21 parameters in both planes, the design process of the edge coupler can be optimised. Firstly, the performance of the edge couplers can be significantly influenced by environmental factors, including temperature fluctuations and humidity. These factors were not integrated into the simulation parameters. As a result, the performance of the coupler under varying environmental conditions is an area that requires further investigation. Including these variables in future simulation models or conducting experimental validations under diverse environmental conditions would be beneficial to ensure the robustness and reliability of the coupler.

The current lens has a focal length of 50 µm. However, it is yet to be determined if a minor alteration in the focal length, for instance, to 47 µm, could potentially improve the couplers performance. Couplers with minor adjustment to the focal length can still be built.

Furthermore, the lens has a tilt limitation ranging from -15° to -35°, within which the focal length remains unchanged. This tilt range allows for compensation of height differences ranging from +2 µm to -1.75 µm. To increase the range of possible tilt angles, the use of an aspheric lens is proposed. Aspheric lenses typically have surfaces that conform to specific forms, as detailed in equation 10. Thereby r describes the displacement of the surface from the vertex. The coefficients α_i describe the deviation of the surface from the axially symmetric quadric surface specified by R and k . By implementing an aspheric lens, the coupler will be capable of compensating for larger height discrepancies between the chips.

$$z(r) = \frac{r^2}{R(1+\sqrt{1-(1+k)\frac{r^2}{R^2}})} + \alpha_4 r^4 + \alpha_6 r^6 + \ldots, [21] \tag{10}$$

9 Outlook

The coupler's design, detailed in Chapter 5, allows the fabrication of the coupler in near future. The construction of this coupler will employ the principle of Direct Laser Writing (DLW). DLW is a 3D photolithography method for creating micro-polymer structurs [22]. This method operates by harnessing a laser beam with a specific wavelength to instigate a particular reaction in a photoresist composed of a photoinitiator and a monomer solution [22]. The optical irradiation causes the photoinitiators to break down into radicals, leading to the polymerization of the monomers. After irradiation, any unutilized photoresist is cleaned off with acetone, leaving only the coupler behind [22].

References

[1] G.W.A. Dummer. Electronic Inventions and Discoveries: Electronics from its earliest beginnings to the present day. CRC Press, 4 edition, 1997. pages 1-43.

[2] Cadence PCB Solutions. Photonic integrated circuits. https://resources.pcb.cadence.com/blog/2023-photonic-integrated-circuits. Accessed: 29 December 2023.

[3] R. Osgood Jr. and X. Meng. Principles of Photonic Integrated Circuits: Materials, Device Physics, Guided Wave Design. Springer, 1st edition, 2021.

[4] X. Guo, J. Xiang, Y. Zhang, and Y. Su. Integrated neuromorphic photonics: Synapses, neurons, and neural networks. Advanced Photonics Research, 2:2000212, 2021.

[5] MIT Media Lab. Mit ai hardware program features ncb research on 2d neuromorphic devices for sustainable artificial intelligence. https://www.media.mit.edu/posts/mit-ai-hardware-program-features-ncb-research-on-2d-neuromorphic-devices-for-sustainable-artificial-intelligence/. Accessed: 2024-01-29.

[6] B. E. A. Saleh and C. Teich, M. Fundamentals of Photonics. Wiley-Interscience, Hoboken, New Jersey, second edition, 2007. pp 1-100.

[7] GoPhotonics. Rayleigh length range calculator. https://www.gophotonics.com/calculators/rayleigh-length-range-calculator. Accessed: 2023-11-05.

[8] Precision Microwave. Understanding tem, te, and tm waveguide modes. https://precisionmmw.com/understanding-tem-te-and-tm-waveguide-modes/. Accessed: 2024-01-25.

[9] C. Xiang, W. Jin, and John E. Bowers. Silicon nitride passive and active photonic integrated circuits: trends and prospects. Photonics Research, 10:A82–A96, 2022.

[10] H. Gehring, A. Eich, C. Schuck, and Wolfram H. P. P. Broadband out-of-plane coupling at visible wavelengths. Optica Publishing Group, pages 1–4, 2019. DOI: Doc. ID 371741.

[11] M. J. Burek, C. Meuwly, and R. E. Evans. Fiber-coupled diamond quantum nanophotonic interface. Physical Review Applied, 8:024026, 2017.

[12] L. Chang, M. Dijkstra, N. Ismail, M. Pollnau, R. M. de Ridder, K. Wörhoff, V. Subramaniam, and J. S. Kanger. Opt. express 23, 22414 (2015). Optics Express, 23:22414, 2015.

[13] R. H. Khandokar, M. Bakaul, M. Asaduzzaman, A. Nirmalathas, and S. Skafidas. Ieee j. quantum electron. 52, 1 (2016). IEEE Journal of Quantum Electronics, 52(1), 2016.

[14] V. R. Almeida, R. R. Panepucci, and M. Lipson. Opt. lett. 28, 1302 (2003). Optics Letters, 28:1302, 2003.

[15] G. Roelkens, D. Vermeulen, D. Van Thourhout, R. Baets, S. Brision, P. Lyan, P. Gautier, and J.-M. Fédéli. Appl. phys. lett. 92 (2008) 13110. Applied Physics Letters, 92:13110, 2008.

[16] A. Delage, S. Janz, D.X. Xu, D. Dalacu, B. Lamontagne, and A. Bogdanov. Proc. of spie. 5577:204, 2004.

[17] V.R. Almeida, R.R. Panepucci, and M. Lipson. Opt. lett. 28 (2004) 1302. Optics Letters, 28:1302, 2004.

[18] Meep Development Team. Meep documentation. https://meep.readthedocs.io. Accessed: 2023-11-05.

[19] Yunfei Fu, Tong Ye, Weijie Tang, and Tao Chu. Efficient adiabatic silicon-on-insulator waveguide taper. Photonics Research, 2:A41–A44, 2014.

[20] W. K. Burns, A. F. Milton, and A. B. Lee. Optical waveguide parabolic coupling horns. Applied Physics Letters, 30(1):28–30, 1977.

[21] F. Lamontagne, U. Fuchs, M. Trabert, and A. Möhl. Aspheric lens mounting. Optical Engineering, 57(10), 2018.

[22] S. Alexandros, Vladimir M., and F. Maria. Direct laser writing: Principles and materials for scaffold 3d printing. Microelectronic Engineering, 132:83–89, 2015.

Erklärung:
Ich versichere, dass ich diese Arbeit selbstständig verfasst und keine anderen als die angegebenen Quellen und Hilfsmittel benutzt habe.
Heidelberg, den 29 jan,
Unterschrift: